Metals and Materials International (2022) 28:307–321
https://doi.org/10.1007/s12540-021-01026-2

Fabrication of Gas Metal Arc Welding Based Wire Plus Arc Additive Manufactured 347 Stainless Steel Structure: Behavioral Analysis Through Experimentation and Finite Element Method

R. Pramod[1] · S. Mohan Kumar[1] · A. Rajesh Kannan[1] · N. Siva Shanmugam[1] · Reza Tangestani[2]

Received: 22 February 2021 / Accepted: 1 April 2021 / Published online: 28 August 2021
© The Korean Institute of Metals and Materials 2021

Abstract
Wire plus arc additive manufacturing (WAAM) technology is utilized to fabricate a 347 stainless steel (SS347) plate using the gas metal arc welding process. The tensile properties of the WAAM plate revealed enhanced strength in comparison with the wrought alloy SS347. The microhardness and the ferrite measurement along the building direction (BD) were in the range of 265–226 $HV_{0.5}$ and 2.2–5.1 FN (Ferrite number), respectively. The microstructural features were comprehensively examined using electron backscatter diffraction (EBSD) analysis and the Inverse pole figure (IPF) maps revealed a strong <001> texture along the BD. Also, well-aligned equiaxed and columnar dendrites with a lower fraction of niobium carbide (NbC) was noticed in the microstructures of the as-built WAAM plate. A three-dimensional finite element model was developed to simulate the build-up of a WAAM plate. Goldak heat source is used to model heat flux in thermal analysis, and the temperature distributions were predicted. Further, residual stress and plastic strain distributions were examined at various stages of the WAAM process.

Keywords WAAM · SS347 · Mechanical properties · Microstructure · Finite element analysis

1 Introduction

The additive manufacturing (AM) process, since its inception in 1986 and first introduced in the manufacturing industry [1], is gaining attention among the industrial and academic sections because of the benefits it offers, such as savings in lead time, economized production costs, and reasonable material savings [2]. In recent times AM is finding rapid advances and applicable usage in various domains such as aerospace, automotive, shipping, medical and construction sectors [3]. Compared to the well-established subtractive manufacturing processes (i.e., machining), intricate components can be inexpensively manufactured by depositing the material (Powder or Filler wire) layer upon layer by progressive consolidation of raw material [4, 5]. WAAM is a type of directed energy deposition process (ASTM F3187-16) used for fabricating near-net-shaped products. In particular, additive metal deposits via the WAAM process uses metal wire as the raw material, plasma arc welding (PAW), GMAW [6, 7], or Gas tungsten arc welding (GTAW) [8] processes for the source of heat, and the manipulation is performed either with a robot or a numerical control unit [9]. The deposition rate utilizing the GMAW process is two–three times higher than GTAW or PAW processes [10]. However, this comes at the expense of bead quality as GMAW process is highly sensitive to slight changes in deposition parameters such as the arc voltage, arc current, welding speed, and deposition rate [11, 12]. In addition, the quality of previous layer influences the layer geometry and the degree of delineations in the as-built structure. The GMAW based WAAM deposition process has considerably lower operational costs, investment and is easy on maintenance in comparison to the electron and laser beam-based WAAM process. Also, there is less risk of porosity formation in relation to the powder-based methods, and it achieves faster speeds than the powder bed AM process [13, 14]. Moreover, arc-based welding systems alter the microstructural characteristics in the fusion zone, by promoting grain refinement and also decreases

✉ N. Siva Shanmugam
nsiva@nitt.edu

1 Department of Mechanical Engineering, National Institute of Technology, Tiruchirappalli, Tamil Nadu 620 015, India

2 Department of Mechanical and Mechatronics Engineering, University of Waterloo, Waterloo, ON N2L 3W8, Canada

or suppresses the porosity formation [15]. In addition, the lower thermal conductivity of stainless steels and the effective shielding arrangement during GMAW process prevents the formation of pores. The GMAW based WAAM process can be easily integrated into a very large operating volume and can achieve a high deposition rate making this technology economical [16]. However, a better conception of the consequent material properties for GMAW based WAAM deposited parts is essential prior to the mass production of components become mainstream.

Structures are fabricated using the commonly available materials such as aluminum [17], stainless steel [12], nickel [4], and titanium [18] deposited via various AM techniques. Wherein, austenitic stainless steels are also deposited, which encompass stable austenitic microstructure, good mechanical properties at elevated temperatures, erosion and corrosion resistant, and excellent weldability finding applications in chemical processing industries and nuclear power plants [19]. SS347 is a stabilized grade due to the presence of Niobium (Nb); further, the amalgamation of NbC decreases the risk of sensitization. A minor amount of NbC intermetallic existing in the candidate material aids in evading the knife line attack during welding [20]. Suryakumar et al. [21] utilized a hybrid layer production technique to deposit mild steel using the GMAW process and introduced a CNC machining operation in-between the next additive deposition layer to fabricate the parts. Also, investigated the anisotropic tensile properties and microhardness of the additive deposits. Jin et al. [22] detailed a comprehensive overview of the WAAM process for industrial applications with stainless steels and explained the influence of process variables on the microstructural characteristics, mechanical properties, and defects associated with AM processed stainless steels. The mechanical integrity of the WAAM processed steel structures is influenced by many factors including the process variables, filler wire composition, shielding gas flow rate and composition, microstructure, and post-heat treatment techniques. To attain high-quality WAAM structures, understanding the process-structure–property relationship along with the evolution of residual stresses during multi-layer deposition is required. In addition, in-situ processes like cold rolling and peening can be employed to reduce the anisotropy problem. Kannan et al. [23] demonstrated the feasibility of manufacturing multi-material structures via WAAM processes using SS904L and Hastelloy C-276. The mechanical properties and metallurgical characterization of the structure were systematically studied, and noticed mechanical properties in-comparison with wrought alloy.

Predicting thermal behavior during the course of the deposition process is crucial for evaluating the microstructures of additive deposits. A three dimensional FE analysis provides a comprehensive insight into the thermo-physical effects undergoing during the additive deposition process. As the additive layers are being repeatedly heated at the same place, FE analysis can be extensively utilized to predict the thermal, residual stress distributions, and stress-induced strain [24, 25]. Saadatmand et al. [26], utilizing the Goldak heat source model, presented a 3D-FE model for predicting the thermal cycle in the course of the WAAM process, also studied the effect of welding speed on the thermal behavior and substrate preheat temperature of low carbon steel-ASTM A36 deposited wall. Ahmed et al. [27] performed FE analysis using Goldak double ellipsoid and a rectangular heat source model by developing a subroutine algorithm. A feasibility study using the two models were made for predicting thermal and residual stress distributions. Ge et al. [24] investigated the thermal history-microstructural evolution-defect distribution in alliance with FE analysis and experimental examination during the WAAM deposition of martensitic stainless steel (2Cr13) structure. The comparative study showed good agreement between the predicted and experimental results. Somashekara et al. [28], a twin-wire welding-based AM utilizing the GMAW process, were developed using experimental methods and FE analysis. FE model aided with two moving heat sources kept at a fixed distance from each other was developed. The material to be deposited was activated by the element birth technique as the arc traveled over the defined trajectory in the model. Further, the validation of residual stress results between the experiment and FE analysis had a good agreement. Pramod et al. [29] fabricated a cold metal transfer-based AA6061-T6 WAAM processed cylinder and studied the mechanical properties and microstructural aspects of the additive deposits. FE analysis of WAAM cylinder consisting of nine layers was modelled using element birth–death technique for predicting the residual stress, strain, and thermal distributions.

From the available literature, only a sparse amount of work has been reported on the use of the GMAW based WAAM process for deposition of ER347 and investigating the mechanical and metallurgical characterization integrated with FE analysis. The present study is aimed at fabricating an additive (layer-by-layer) deposition plate of ER347 on the SS347 substrate using the WAAM process. The mechanical properties and metallurgical observations for the GMAW based WAAM processed additive deposited plate is detailed. FE analysis using a Goldak heat source is implemented to predict the residual stresses, strain, and temperature history during the WAAM process.

2 Experimentation

The ER347 feedstock wire having a diameter of 1.2 mm was deposited on 12 mm thick substrate material (SS347) via GMAW based OTC Daihen FD-B6 robot, as shown in

Fig. 1a. The chemical composition of the filler wire and substrate is presented in Table 1.

The deposition strategy was in a back and forth motion, as this type of sequence will avoid the end crater formation and uniform bead height can be achieved with less amount of delineations. The welding parameters were considered from a numerous trial and error experiments by varying the process variables such as welding current, wire feed rate and welding speed. The selected parameters are as follows: Welding current-190 Amps, Welding speed-350 mm/min, Welding voltage-17.70 V, Wire feed rate-6.56 m/min, Shielding gas (98% Argon + 2% CO_2) with a constant flow rate of 20 l/min. A dwell time of 60 s was introduced between successive deposition of additive layers. Twenty additive layers were deposited, as shown in Fig. 1b, the dimensions of the manufactured additive plate are measured 150 mm × 110 mm × 8 mm. The additive deposited plate was further face milled, and the final dimensions are measured 130 mm × 100 mm × 5 mm.

2.1 Sample Preparation and Testing

A wire-cut electrical discharge machine was used to prepare the specimens for metallographic examination and implemented standard metallographic techniques according to ASTM E3-11 (2017). WAAM microstructure was observed utilizing Hitachi 4300 SE/N Field Emission Scanning Electron Microscopy (FESEM) fitted with OIM software and EBSD detector. IPF, phase distribution, and grain size distribution maps were obtained from EBSD analysis. Tensile specimens were prepared in accordance with ASTM E8/E8M-16ae1, and a test was conducted using Instron make: 8801 (100kN) universal testing machine (refer to Fig. 1c) at room temperature (25°) with a 1 mm/min loading rate. To investigate the anisotropic properties along the deposition direction, the three samples were tested for each of the three orientation angles (0°, 45°, and 90°), and an average tensile strength value is noted. The bend sample is prepared according to ASTM E190-14. A Wilson make 402 MVD system was utilized to document the average microhardness measurements for the WAAM plate by performing three indentations at each point with a test force of 500 gf, dwell time 10 s, and 0.5 mm between indentations (ASTM E92-17).

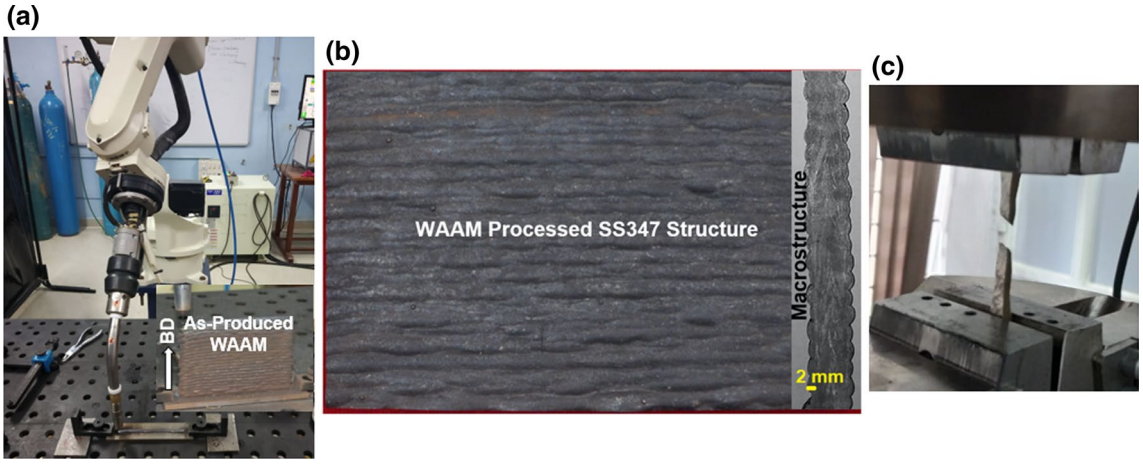

Fig. 1 WAAM processing sequence: **a** GMAW robotic welding setup, **b** As-deposited WAAM plate with macrostructure, and **c** WAAM sample subjected to uniaxial tensile test

Table 1 Chemical composition (wt%) for ER347, and AISI 347

Alloys / Element	Fe	Si	Ti	Cu	C	Mo	Mn
AISI 347	70.002	0.360	0.007	0.257	0.030	0.085	1.460
ER347	67.229	0.420	0.007	0.230	0.060	0.320	1.650
Alloys/Element	Cr	V	Ni	Nb	S	W	P
AISI 347	17.130	0.041	10.080	0.510	0.001	0.017	0.020
ER347	19.800	0.041	10.200	0.600	0.001	0.017	0.025

3 Thermo-Mechanical FE Analysis

A three dimensional FE modelling of the WAAM plate is performed using ABAQUS 2017 software. Struers welding expert system was utilized to measure the average thickness of individual layers from the macrostructure examination. A coupled thermo-mechanical analysis is selected wherein the thermal analysis (heat transfer step) is solved first to record the nodal temperature distributions. Further, for an individual node, the achieved temperature results (from the thermal analysis) are utilized as a thermal load in the subsequent mechanical analysis (static, general step) to note the residual stress and strain results. The material deposition is executed by an individual element activation algorithm by means of the element birth method. The elements were deactivated initially in the first step and then activated sequentially by following the movement of the arc or heat source [30, 31]. The deposition is carried out by laying the individual weld bead, and 60 s of dwell time is assigned at the termination of each layer. The dwell time allowed the layers to cool down prior to new layers being deposited. A heat source model is utilized to simulate the transfer of heat from the arc to the weld pool, which defines the heat generation per unit volume in the weld pool region [32]. In the heat transfer step, the moving heat source is developed by using a user subroutine DFLUX code in the ABAQUS software, and the Goldak heat source [33] was employed to model the heat flux in thermal analysis. The power density distribution for the area which is in front of the arc center is defined using Equation-1, and similarly for the area which is behind the arc center is defined using Equation-2 as shown below:

$$q_f = \frac{6\sqrt{3}Qf_f}{\pi\sqrt{\pi}a_f bc} e^{\left[-3\left(\frac{x^2}{a_f^2}+\frac{y^2}{b^2}+\frac{z^2}{c^2}\right)\right]} \tag{1}$$

$$q_r = \frac{6\sqrt{3}Qf_r}{\pi\sqrt{\pi}a_r bc} e^{\left[-3\left(\frac{x^2}{a_r^2}+\frac{y^2}{b^2}+\frac{z^2}{c^2}\right)\right]} \tag{2}$$

$$f_f + f_r = 2 \tag{3}$$

where, x is the longitudinal, y is the lateral, and z is the normal dimensions. The length of the front ellipsoid (a_f) and length of the rear ellipsoid (a_r). Width of the heat source (b), depth of the heat source (c); Q is the energy input considering the factor of efficiency. The schematic representation for the terms are presented in Fig. 2a, b depicts the heat source modelling in FE analysis. The factors for heat deposition to the front and rear of the heat source is represented by f_f and f_r respectively. The distinct parameters utilized for the Goldak heat source model [34, 35] are presented in Table 2.

The material properties assigned to the model are temperature-dependent, which constitutes thermo-mechanical and thermo-physical properties; the material data is adopted from the literature Kim et al. [36]. An assumption in relation to the convection coefficient and emissivity values, which are regarded to be independent of the temperature and assigned 5.7 $Wm^{-2}K^{-1}$ and 0.2 respectively [34]. The boundary condition for the heat transfer step included initial temperature at 25°C, and for the mechanical analysis, the substrate was clamped to restrict its movement in all degrees of freedom. The mesh elements constituted

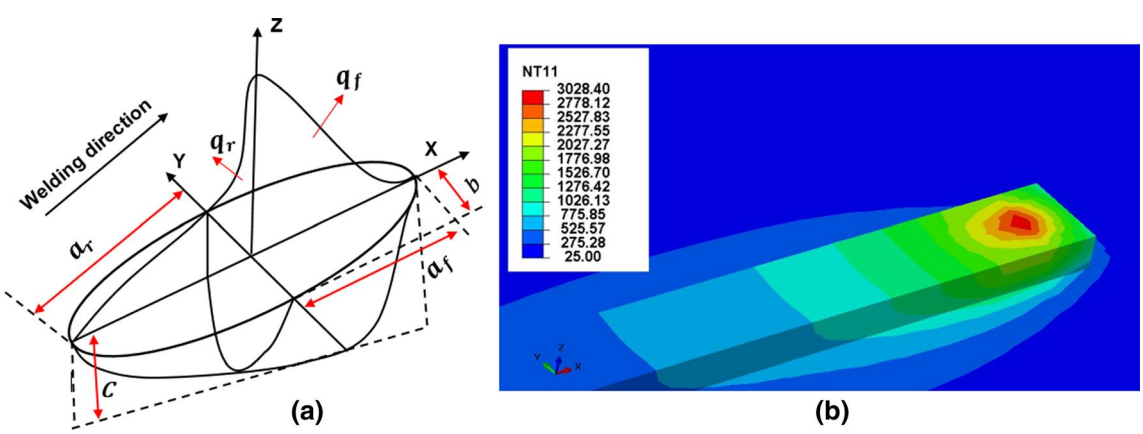

Fig. 2 Representation of Goldak heat source model: **a** Schematic illustration, and **b** FE analysis

Table 2 Goldak heat source model parameters

a_f, mm	a_r, mm	f_f	f_r	b, mm	c, mm	Q, Watts
2	6	0.6	1.4	2.5	3	2245.83

DC3D8 for heat transfer analysis and C3D8R for structural analysis with 36, 3, and 3 elements in the X, Y, and Z directions, respectively. Each additive layer ensured precise results based on the mesh convergence test (refer to Fig. 3). The additive layers were fine-meshed with a total number of 4474 elements, while a slightly coarse mesh with a total number of 781 elements was assigned for the substrate to reduce the simulation time, and the aspect ratio of 1 is selected for the element size.

4 Results and Discussion

4.1 Mechanical Properties and Microstructural Examination

Figure 4 and Table 3 presents the tensile properties of as-built (AB) and wrought counterparts. The WAAM samples exhibited better tensile properties in comparison to base metal (BM) at different orientations. The AB WAAM sample at 45° orientation showed better tensile properties compared to specimens at 0° and 90°, i.e., tensile strength-UTS,

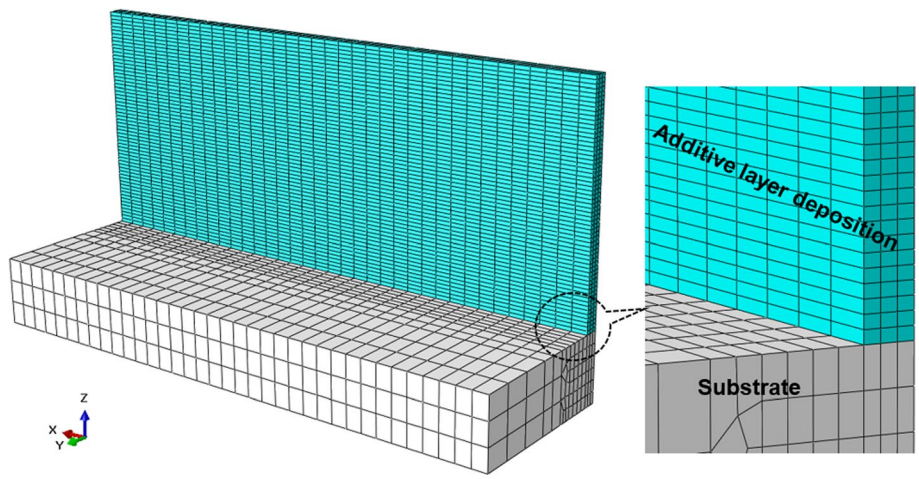

Fig. 3 Mesh representation for the modelled WAAM structure

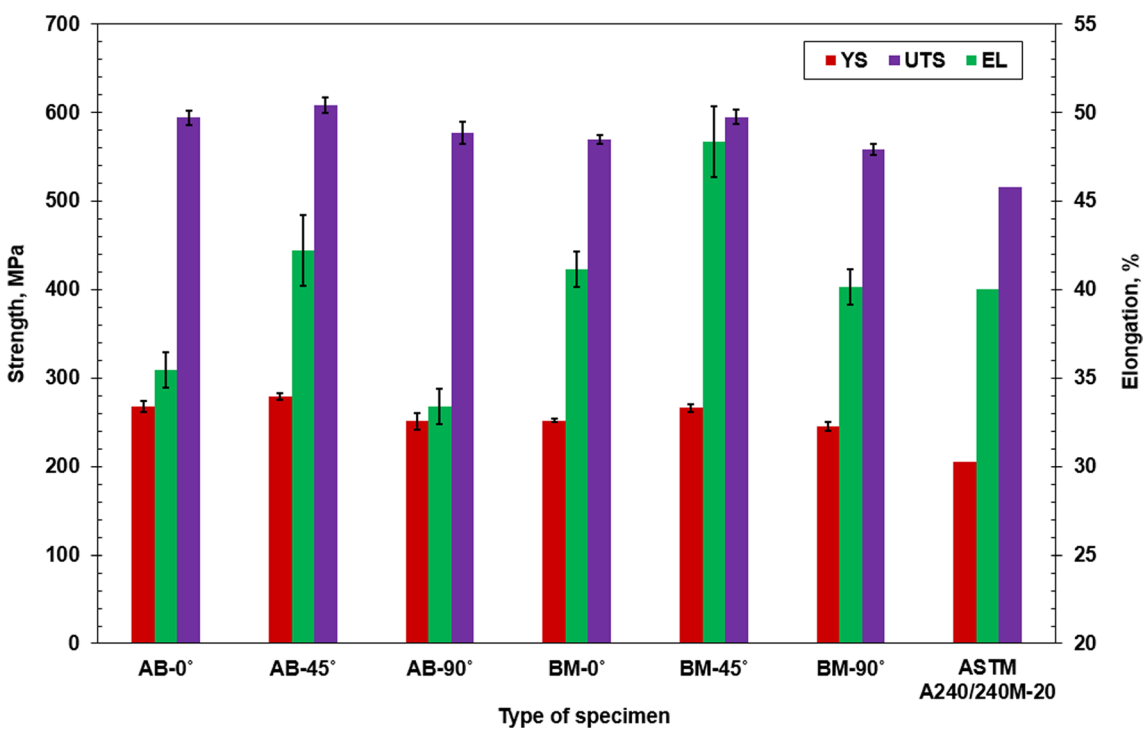

Fig. 4 Anisotropic tensile properties of WAAM samples and wrought alloy

Table 3 Tensile test results for WAAM plate and wrought alloy

Type of specimen	YS, MPa	UTS, MPa	EL, %
AB-0º	268 ± 6	594 ± 8	35.44 ± 1
AB-45º	279 ± 4	608 ± 9	42.21 ± 2
AB-90º	251 ± 9	577 ± 13	33.37 ± 1
BM-0º	252 ± 2	570 ± 5	41.12 ± 1
BM-45º	266 ± 4	595 ± 8	48.33 ± 2
BM-90º	245 ± 5	558 ± 6	40.15 ± 1
ASTM A240/A 240M-20A [40]	205	515	40

yield strength-YS, and percentage of elongation-EL were 608 MPa, 279 MPa, and 42.21%, respectively. Similarly, BM samples at 45º orientation yielded better tensile properties than that of the specimens at 0° and 90° orientations, i.e., UTS, YS and EL are 595 MPa, 266 MPa, and 48.33%, respectively. This variation in the tensile properties is attributed to a difference in the effective mean free path on which dislocations can move in different directions, with grain boundaries limiting the dislocation movement and acting as barriers in the so-called "Hall–Petch" type strengthening phenomenon [37]. In addition, the tensile strength is influenced by the mechanical fibering and crystallographic characteristics caused by the ferrite concentration in the WAAM processed structure [38, 39]. As observed from Fig. 4, the tensile properties of the WAAM specimens at different orientations were comparable to wrought counterparts and conforms to ASTM A240/A240M-20a requirements [40]. The comparable tensile strength and reduced ductility of WAAM specimens are corroborated to the dendritic microstructure along with an increased fraction of ferrite (2.2–5.1 FN). Bhadeshia [41] reported that the welded stainless steel specimens exhibited an increase in UTS at room temperature due to the formation of residual delta-ferrite. These retained residual delta-ferrite accommodates contraction strains elastically and aids in improving tensile strength while austenite deforms plastically. i.e., more tensile stresses in austenite and compressive stresses in ferrite arise during the transformation of austenite to ferrite in the deposited layer. The ferrite measurements using Feritscope (Make: Fischer FMP30) revealed the varying concentration of ferrite along the BD and were in the range of 2.2 to 5.1 FN. Moreover, from the previous research work, parts produced using other AM processes also revealed the anisotropy problem [42, 43].

The microstructural variation and its impact on the material properties were correlated using the Vickers microhardness test. The measurements were made at three distinct regions of the WAAM plate, i.e., top, middle, and bottom, values are provided in Fig. 5. The higher hardness value of the WAAM plate confirms the existence of delta ferrite and NbC (refer to Fig. 8) in the fabricated WAAM plate [44]. The highest hardness (265 ± 4 $HV_{0.5}$) value is recorded at the bottom section of the WAAM plate, with an average hardness value of 246.33 $HV_{0.5}$. The mean hardness at the middle and top regions were 248 ± 7 and 226 ± 6 $HV_{0.5,}$ respectively. The hardness values along the BD were higher than the wrought counterpart and conforms to hardness requirements specified in ASTM A240/A 240 M-20A [40]. A gradual increase in the microhardness values was noticed from the top to bottom region of the WAAM plate. The steady change in microhardness values is attributed to varying complex cyclic thermal history (CCTH) during the WAAM process. It is also observed that with a decrease in ferrite concentration along the building direction, the hardness shows a decreasing trend [45–47]. The WAAM sample was subjected to a bend test, and Fig. 6 represents the sample after the completion of the bend test. The specimen indicated no evidence of cracks, fissures, or openings in the bent region and endured the 180° bend, signifying acceptable ductility.

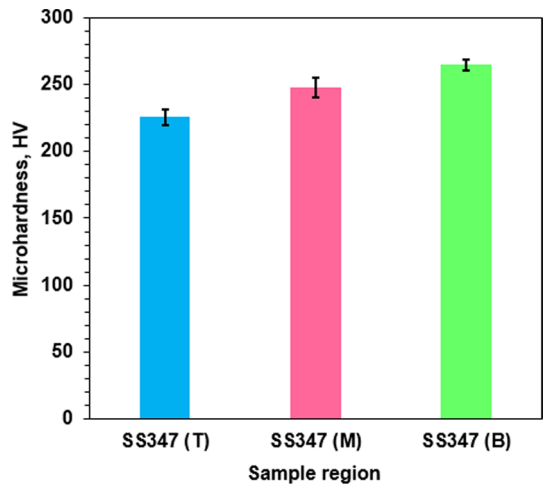

Fig. 5 Microhardness measurement from bottom to top region in WAAM plate

Fig. 6 Bend test result of WAAM specimen

Figure 7 represents the microstructural characteristics for the WAAM plate alongside the built-up direction. The EBSD IPF maps disclosed a strong <001> texture, as <001> is the easy growth direction for FCC materials such as austenitic stainless steels during the WAAM process along the BD as depicted in Fig. 7a, d, g [48]. The preferred crystallographic texture <001> and <100> belongs to the {100} family of FCC materials and mainly occurs during the formation of columnar and equiaxed dendrites in fusion-based welding processes [49, 50]. Microstructure reveals that grains are generally oriented in <001> and <101>, and this highlights the decreased ductility of WAAM based structures, as reported in available literature [51]. As the layer height increases, the microstructure turns coarse, comprising of austenitic columnar grains, and nucleated epitaxially at the interface of layer boundary. Many researchers have stated the formation of columnar dendrites parallel to the built-up direction [52]. A dendritic microstructure is formed during the process of WAAM deposition, as the molten pool fully directionally solidify and develop into dendrites along the BD, thus in good agreement with the solidification theory of FCC materials. A slight increase in dendrite size is witnessed from the bottom to top region of the WAAM plate. An EBSD phase distribution analysis (Fig. 7b, e, h) indicated the existence of austenite and ferrite phases in the WAAAM plate. The ferrite fraction in the bottom, middle, and top sections were noted 5.1%, 3%, and 2.2%, respectively.

The increased ferrite fraction is because of the increase in retained residual-delta ferrite in the course of deposition and as an outcome of rapid solidification. The cooling rate also affects the microstructure of the as-built plate, and in turn, it influences the mechanical integrity. The microstructure at the bottom region of the AB plate comprised of fine equiaxed dendrites owing to rapid cooling, as the heat was dissipated rapidly to the substrate with a higher cooling rate (Fig. 7g). As the height of the WAAM plate increases, the solidification time also increases, i.e., lower cooling rate. A coarse dendritic microstructure is observed as the heat is dissipated to the surroundings; thereby, the cooling rate decreases (Fig. 7a, d). As reported by Rodrigues et al. [5], cooling rate controls the formation of various phases during multi-layer deposition and calculated the cooling rates by

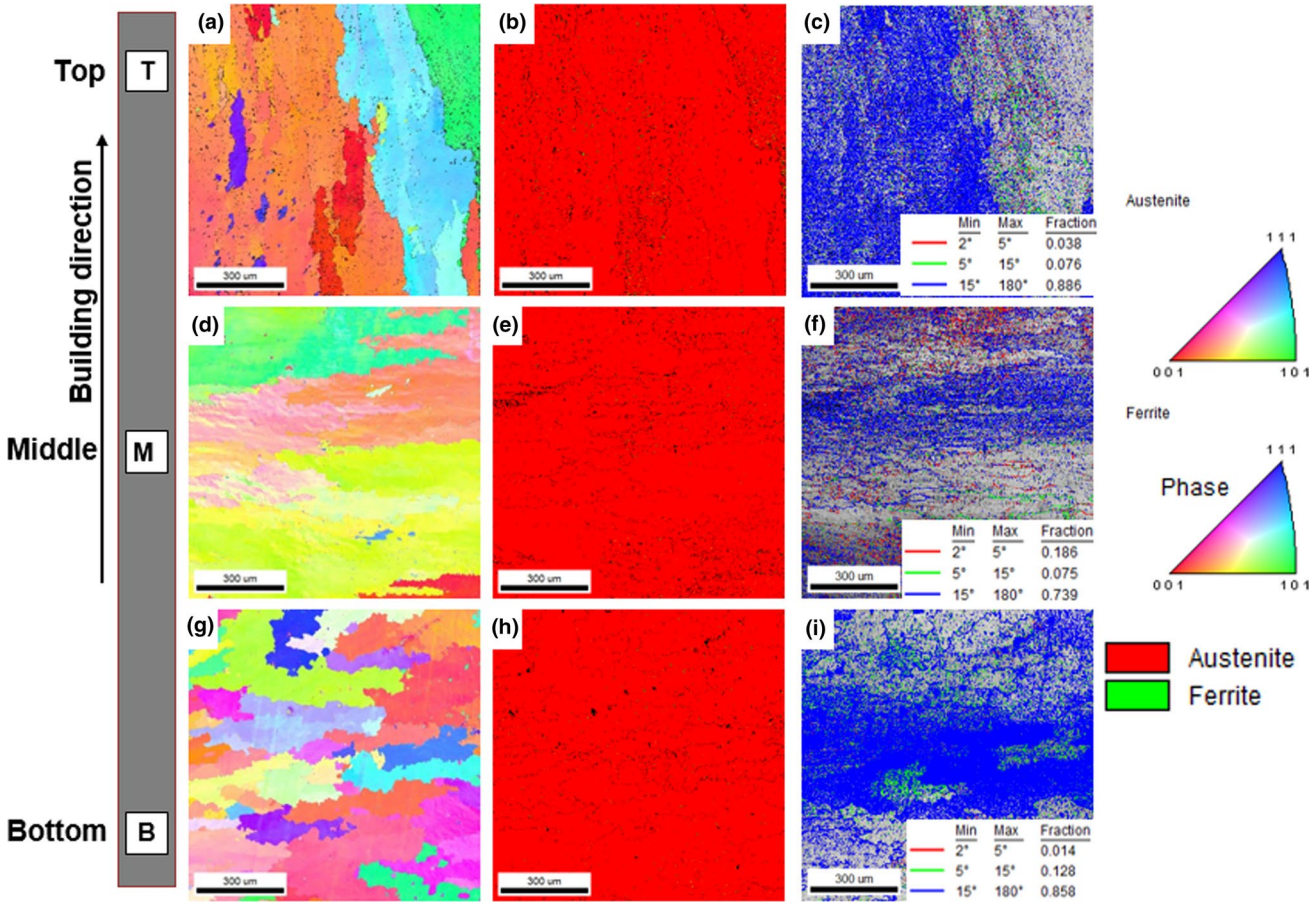

Fig. 7 Microstructural evolution of WAAM plate at different locations along the BD: EBSD IPF map (**a**, **d**, **g**), phase distribution map (**b**, **e**, **h**), and grain boundary distribution map (**c**, **f**, **i**) at the top (T), middle (M), and bottom (B)

evaluating the average temperature gradient in the range of 800 to 500 °C ($t_{8/5}$), as this temperature regime has a substantial effect on the microstructure of stainless steel. The cooling rate was in the range of 50 to 60 °C in the bottom regions, i.e., the heat dissipated into the substrate during the deposition of initial layers, resulting in higher cooling rates. With increasing layer height, the heat dissipated into the previous deposited layers and to the atmosphere with lower cooling rate (5 to 20 °C). Hence higher ferrite fraction is observed in the bottom layers in comparison to middle and top layers. These observations are in line with the EBSD results reported on the WAAM processed stainless steel structures [53–56]. The microstructural variation along the building direction is attributed to the varying CCTH during the WAAM process [57]. The existence of well-aligned dendrites (equiaxed and columnar) in the WAAM plate. Figure 7c, f, i depicts the distribution of Low Angle Grain Boundaries (LABs) and High Angle Grain Boundaries (HABs) at various locations of the WAAM plate along the BD. Examining the grain boundary maps, it can be noted that major portions of the grain boundaries are HABs. The higher fraction of HABs (refer to Table 4) is credited to rapid solidification during the WAAM process and helps in the development of new grains and a refined microstructure [58].

Figure 8 reveals the presence of NbC in the WAAM plate. The Energy-dispersive X-ray spectroscopy (EDS) line scan elemental plot shows that Fe and Cr peaks are more concentrated in the WAAM sample than other elements. The increase in Nb peak with a decrease in Fe and Cr reveals the presence of NbC in the WAAM Plate, and these NbC particles will avoid the knife line attack and works as a nucleation site for grain growth [39, 44]. For SS347 containing 0.059 wt% C and 0.64 wt% Nb, the fraction of NbC will be very low and the precipitation of $M_{23}C_6$ is obstructed during multi-pass welding [59].

4.2 Finite Element Analysis

The distributions of nodal temperature (NT11), residual stress, and plastic strain (PE) are investigated at various phases of the additive layer deposition, i.e., the first, tenth, and twentieth layers. The first layer of deposition is similar to the bead on plate welding trials. As the additive deposition is initiated, the molten pool gradually starts to develop. Further, as the heat source moves, the elements get activated along the deposition track. The evolution of the temperature distribution, Von-Mises stress, and plastic strain of multilayer additive depositions are presented when the heat source is at the midpoints of the first (refer Fig. 9a–c), tenth (refer Fig. 10a–c), and twentieth (refer to Fig. 11a–c) layer. Similarly, at the termination of the cooling period, the temperature distribution, Von-Mises stress, and plastic strain is presented for the first (refer to Fig. 9d–f), tenth (refer Fig. 10d–f), and twentieth (refer to Fig. 11d–f) layer. A peak temperature of 3210°C, Von Mises stress of 644 MPa, and corresponding plastic strain of 0.0049% are witnessed at the deposition of the first layer as it is subjected to faster heating and cooling cycles. Also, thermal gradients are higher at the initial metal deposition because of the ambient room temperature [60]. During the first layer deposition, the heat flow to the substrate is also higher, and the heat accumulation in additive deposits is less. With the addition of layers and an increase in the height of the WAAM plate, the heat input from the heat source becomes greater than heat loss leading to thermal accumulation in the WAAM structure [25]. The size and shape of the molten pool will not change much after the first layup, and the melt pool reaches a quasi-stationary state since the input welding parameters are constant [9]. At the completion of dwell time of 60 s for the first layer, the peak temperature reduces to 109°C, and the heat is effectively dissipated to the substrate. The molten pool comprises of metal in the liquid state, resulting in a zero-stress state in the weld pool. The metal slightly away from the molten pool surrounding starts to expand due to thermal flux and develops a compressive stress state, and results in a higher stress state at the adjoining areas of the heat source path [61]. When the heat source is located at the middle section of the first layer, the maximum Von Mises stress is observed at the arc starting point. Further, after the dwell period and the layer gets cooled, an increase in equivalent stress (746 MPa) and plastic strain (0.005%) is noticed. This is attributed to a decline in temperature resulting in cooling and shrinkage, which leads to a surge in the equivalent stress and strain state.

During the deposition process of adding new layers, the earlier deposited layer gets subjected to reheating and remelting resulting in an effect of stress relief; this is because the addition of new layers is similar to imparting a cycle of low-temperature heat treatment on the previously deposited layer [62]. Also, throughout the deposition process, the stress developed by the fore layer is released due to the heat imparted by the rear layer. During WAAM, two regions near the arc start and endpoint are in a larger equivalent stress state. The direction of deposition is to-and-fro motion, so as the heat source travels to the arc endpoint, the region nearby it has a small stress state because of the

Table 4 LABs and HABs of different regions

Region	LABs, %		HABs, %
	$2° \le \theta \le 5°$	$5° \le \theta \le 15°$	$15° \le \theta \le 180°$
Top	3.8	7.6	88.6
Middle	18.6	7.5	73.9
Bottom	1.4	12.8	85.8

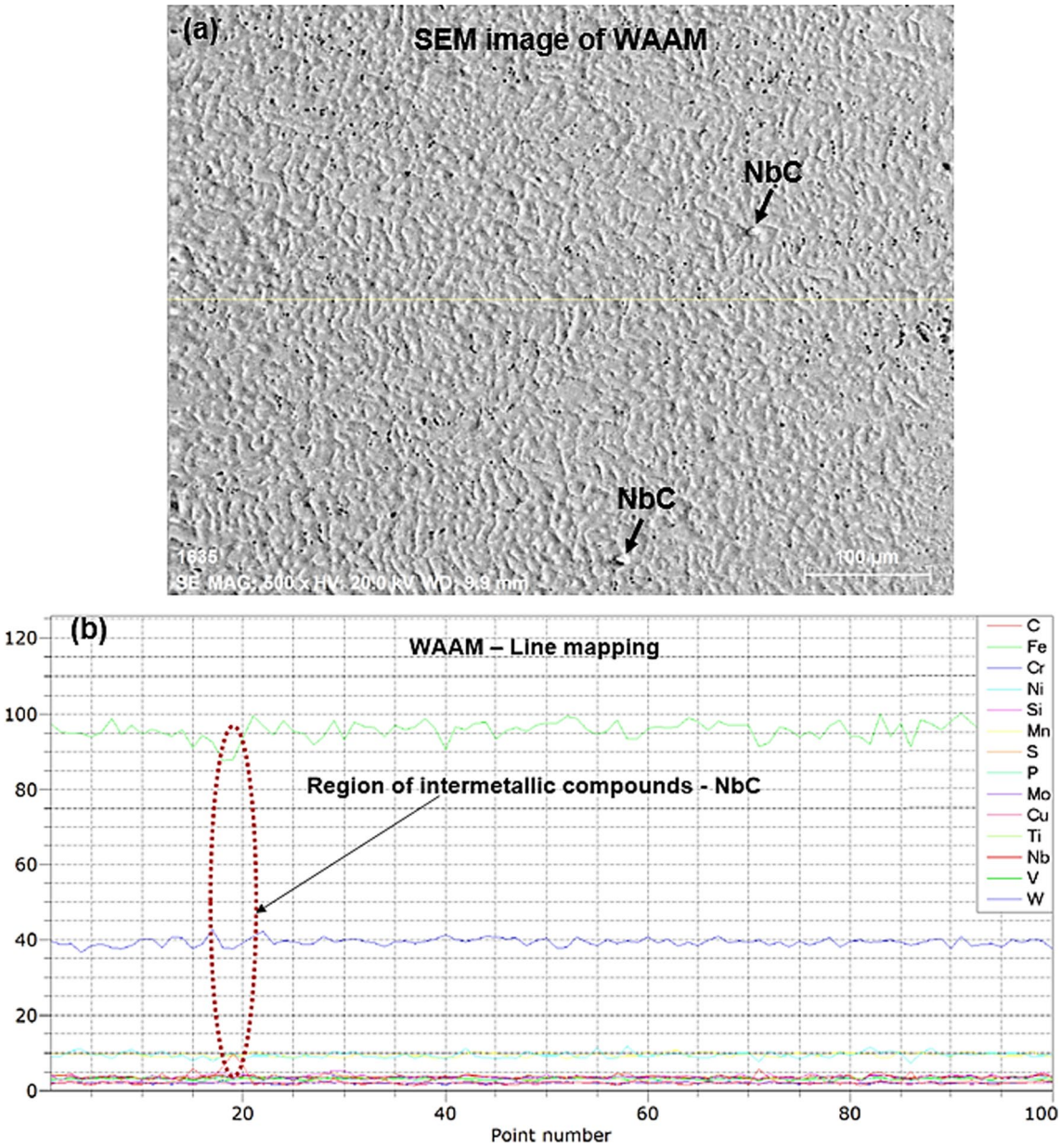

Fig. 8 EDS line scan result

thermal effect induced by the heat source. In this condition, the region near the arc start point has a large stress state and vice-versa. Thus, for the WAAM process, the equivalent stresses in the vicinity of the start arc and the end arc points alternately increase and decrease depending on the deposition pattern [61]. After the addition of numerous layers, the deposition process gets stabilized; it is noted that the highest temperature of 3049°C (refer Fig. 10a) and 3040°C (refer Fig. 11a) is noticed as the heat source is present at mid-region of the tenth and twentieth layer of deposition respectively. Correspondingly, the cooling pattern is also noted similar with 136°C (refer Fig. 10d) and 167°C (refer Fig. 11 d) for the WAAM plate for the tenth and twentieth layer of deposition, respectively.

The temperature rises non-linearly alongside the Z-direction as the WAAM plate experiences twenty different heat treatment cycles during the deposition process. The peak Von-Mises stress and plastic strain is predominantly observed in the substrate for the tenth and twentieth layer (refer to Fig. 10b, c and Fig. 11b, c). This is attributed to the transfer of heat from the top layer to the substrate and keeping dwell time in between the additions of each layer initiates a stress release effect. With an increase in plate height, the influence of the heat source on bottom layers reduces.

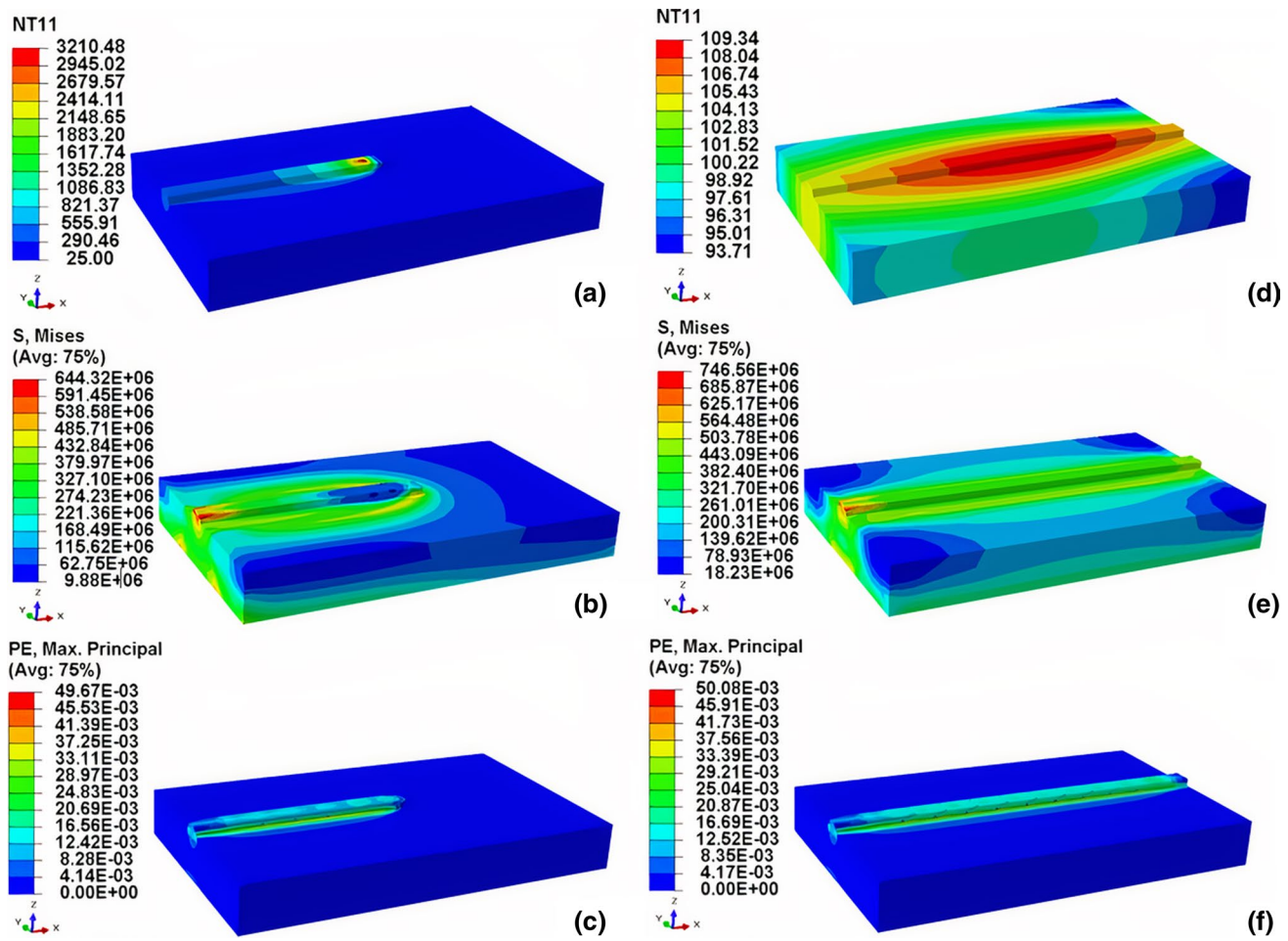

Fig. 9 Layer deposition at mid-length, and at the completion of the first layer in WAAM plate **a**, **d** nodal temperature, **b**, **e** Von Mises stress, and **c**, **f** plastic strain distribution

When the temperature of the WAAM plate reaches ambient temperature, the equivalent stress converts to residual stress [61]. As depicted in Figs. 10e and 11e, the equivalent residual stresses of deposited layers are nearly uniform, barring the local area. The distribution of plastic strain for the tenth and twentieth layer after cooling was similar, as shown in Figs. 10f and 11f, with a gradual rise in strain percentage as the number of layers are deposited. Xi et al. [63] reported that due to the addition of layers and application of dwell time, the part gradually starts to contracts inwards, which had previously deformed outward during the depositing process.

When the predicted peak temperature value exceeds the melting point temperature of the material (1398–1446°C for ER347), at any given stage of material deposition, the metal gets melted, and the molten metal is laid on the substrate for the first layer, and subsequent additive layered deposits. With the ongoing progress of the WAAM process, the heat starts to accumulate in the layered deposits due to the continuous supply of thermal influx and a decrease in the average cooling rate. This thermal accumulation is shown in Fig. 12a, where the source of heat in the GMAW process and Goldak heat source model is compared during the deposition process, and also, the thermal accumulation in the prior layers is evident. Further, during the initial stages of the cooling period, the comparison of temperature distribution and cooling behavior between the experimental and FE analysis is represented in Fig. 12b, which are identical.

The temperature distributions along the deposition direction for the additive layer deposits were noted for the fifth, tenth, fifteenth, and twentieth layer. Figure 13 displays the characteristic plot of temperature vs. distance along the deposition path at the mid-points of each layer. The typical behavior did not reveal any major variation for the temperature history among the additive deposited layers. The peak temperature noticed across the layers specifies the re-melting occurring in additive layers helping in the better interlayer bonding. This phenomenon can refine the microstructure and result in enhanced mechanical strength of the WAAM plate [64].

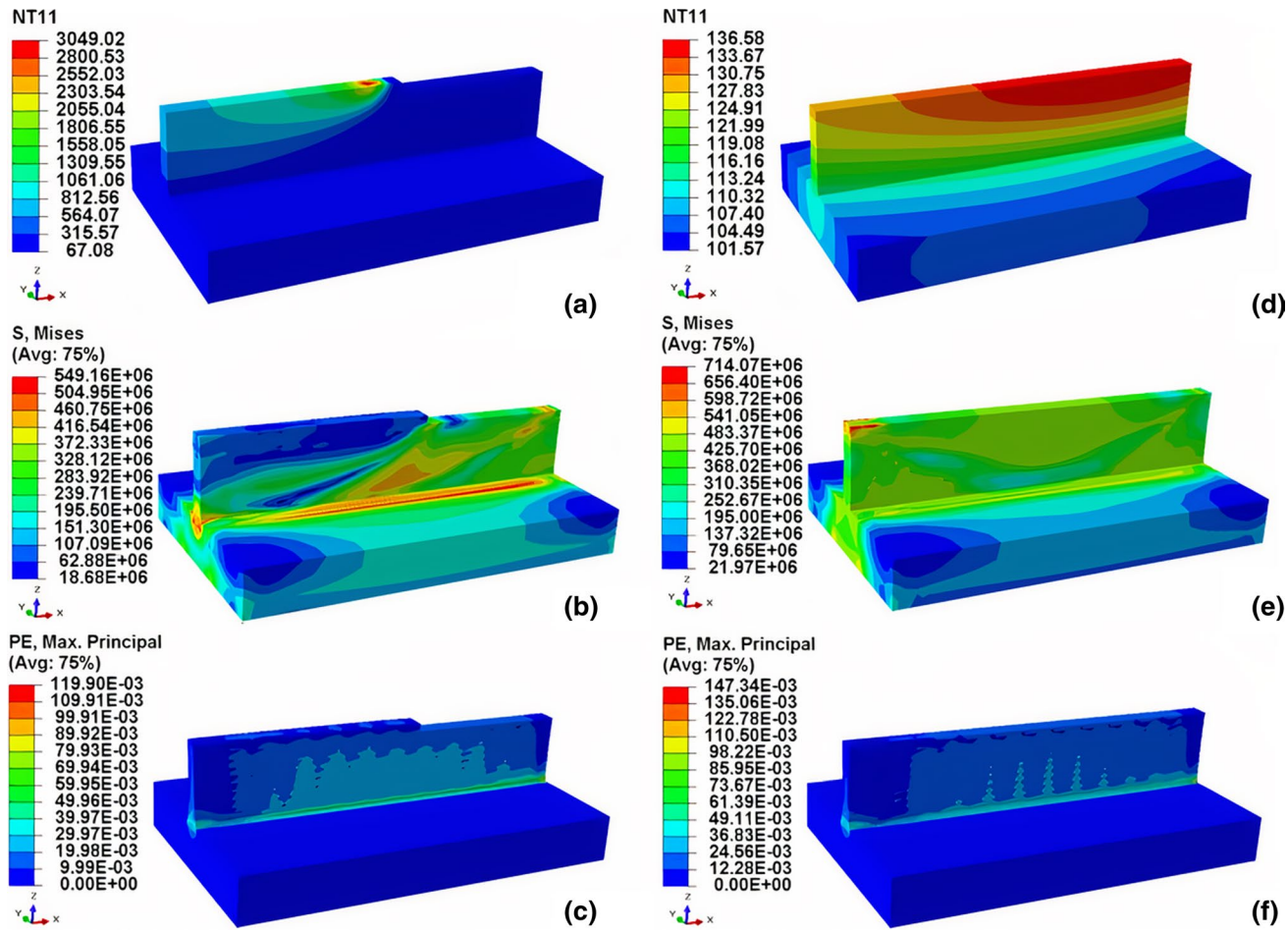

Fig. 10 Layer deposition at mid-length, and at the completion of the tenth layer in WAAM plate **a**, **d** nodal temperature, **b**, **e** Von Mises stress, and **c**, **f** plastic strain distribution

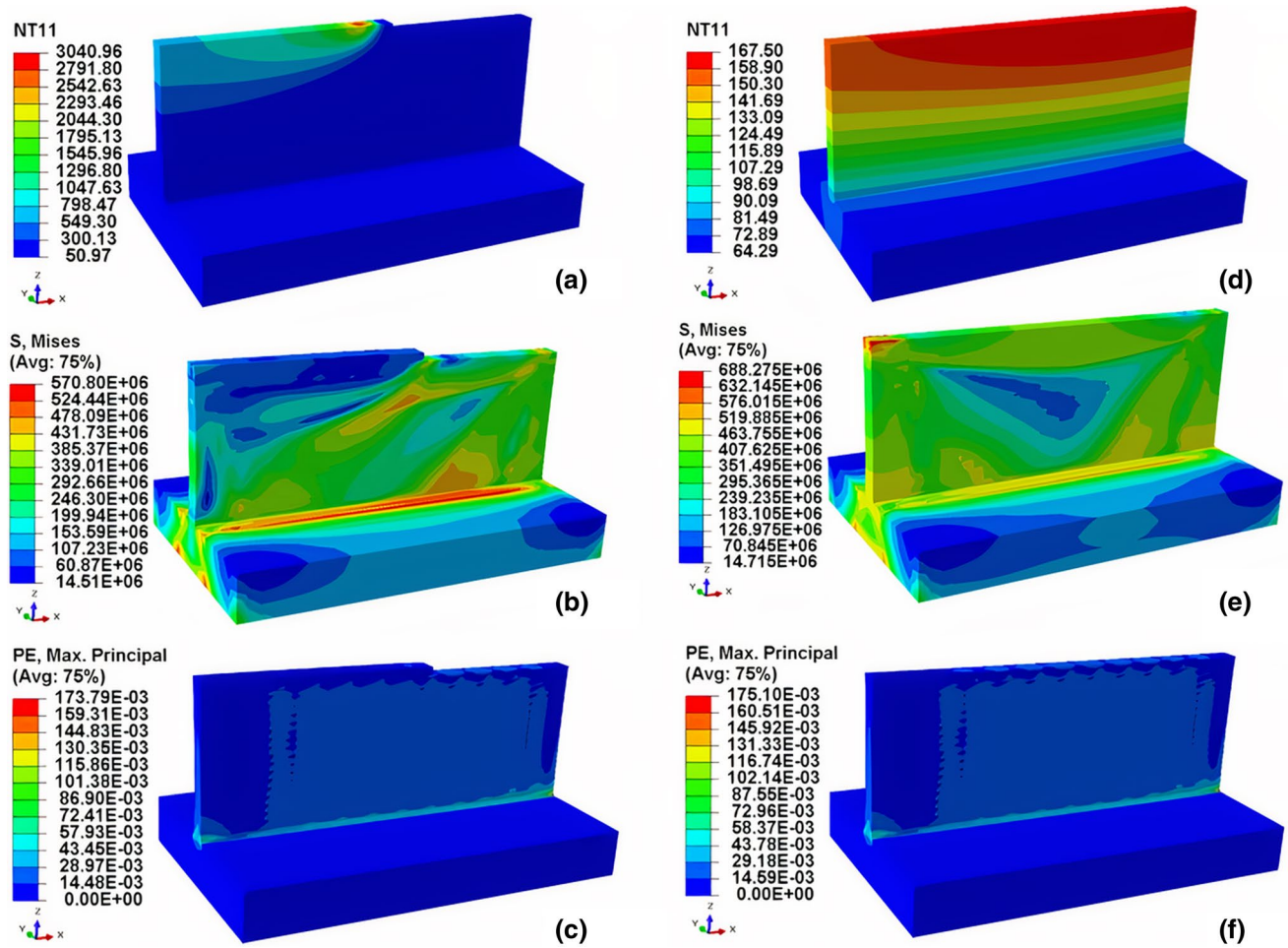

Fig. 11 Layer deposition at mid-length and at the completion of the twentieth layer in WAAM plate **a**, **d** nodal temperature, **b**, **e** Von Mises stress, and **c**, **f** plastic strain distribution

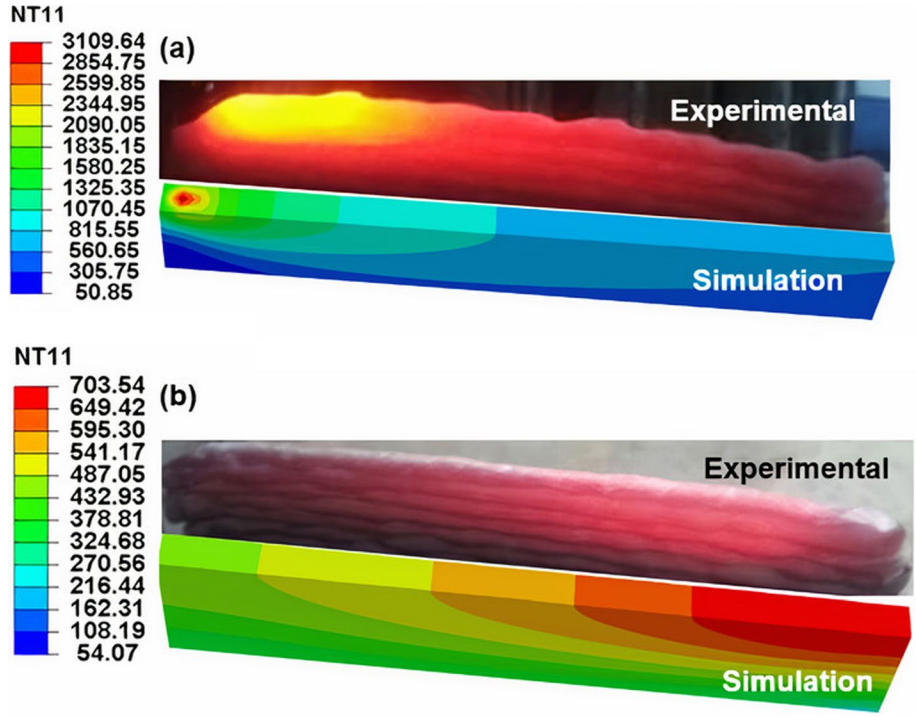

Fig. 12 Heat source comparison between experimental and FE analysis: **a** during the deposition, and **b** the cooling phase

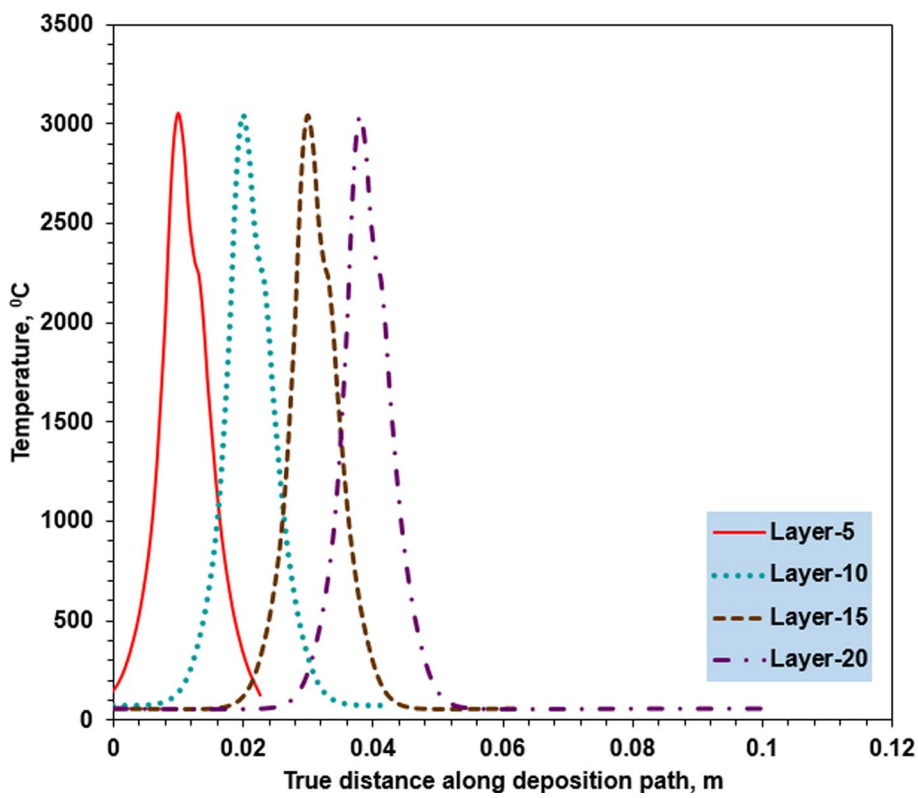

Fig. 13 Graphical representation of temperature versus distance along the deposition path for fifth, tenth, fifteenth, and twentieth layers

5 Conclusions

In the present study, utilizing the robotic GMAW process, a WAAM component was successfully fabricated. Experimental investigation and FE analysis studies were performed, and the main conclusions are made as follows:

The microstructure and mechanical properties of the WAAM plate are comparable with industrial requirements.

The austenite phase presented <001> and <101> orientations in the BD of the as-deposited WAAM plate. The <001> and <100> are the preferred growth direction for FCC materials during fusion-based welding processes.

The higher fraction of HABs is due to rapid solidification and recrystallization during the WAAM process.

The WAAM specimen subjected to bend test showed no signs of cracks, fissures in the bend region.

The thermal behavior of the multilayer WAAM process was studied using the Goldak heat source model, and the FE simulation aided in investigating the temperature distribution, residual stress, and plastic strain measurement in detail. Also, these results were analyzed for the first, tenth, and twentieth layer of the WAAM plate.

The effect of thermal heating and residual stress on the deposited layers are briefly analyzed.

The re-melting phenomenon is observed between adjacent layers of additive deposits and projecting an inter-layer metallurgical bonding of the WAAM plate.

Declaration

Conflict of interest The authors declare that they have no conflict of interest.

References

1. D.S. Choi, S.H. Lee, B.S. Shin, K.H. Whang, Y.A. Song, S.H. Park, H.S. Jee, J. Mater. Process. Tech. **113**, 273 (2001)
2. N. Jeyaprakash, C.H. Yang, K.R. Ramkumar, Met. Mater. Int. (2021). https://doi.org/10.1007/s12540-020-00933-0
3. E. Karayel, Y. Bozkurt, J. Mater. Res. Technol. **9**, 11424 (2020)
4. Y. Ma, D. Cuiuri, C. Shen, H. Li, Z. Pan, Addit. Manuf. **8**, 71 (2015)
5. K. Benarji, Y.R. Kumar, A.N. Jinoop, C.P. Paul, K.S. Bindra, Met. Mater. Int. **27**, 488 (2021)
6. T.A. Rodrigues, V.R. Duarte, D. Tomás, J.A. Avila, J.D. Escobar, E. Rossinyol, N. Schell, T.G. Santos, J.P. Oliveira, Addit. Manuf. **34**, 101200 (2020)
7. J.G. Lopes, C.M. Machado, V.R. Duarte, T.A. Rodrigues, T.G. Santos, J.P. Oliveira, J. Manuf. Process. **59**, 739 (2020)
8. Z. Zeng, B.Q. Cong, J.P. Oliveira, W.C. Ke, N. Schell, B. Peng, Z.W. Qi, F.G. Ge, W. Zhang, S.S. Ao, Addit. Manuf. **32**, 101051 (2020)
9. X. Bai, P. Colegrove, J. Ding, X. Zhou, C. Diao, P. Bridgeman, J.R. Hönnige, H. Zhang, S. Williams, Int. J. Heat Mass Tran. **124**, 504 (2018)
10. D. Ding, Z. Pan, D. Cuiuri, H. Li, Int. J. Adv. Manuf. Tech. **81**, 465 (2015)
11. J. Xiong, G. Zhang, J. Mater. Process. Tech. **214**, 962 (2014)
12. B. Parvaresh, R. Salehan, R. Miresmaeili, Met. Mater. Int. **27**, 92 (2021)
13. C.V. Haden, G. Zeng, F.M. Carter III., C. Ruhl, B.A. Krick, D.G. Harlow, Addit. Manuf. **16**, 115 (2017)
14. C. Shen, Z. Pan, Y. Ma, D. Cuiuri, H. Li, Addit. Manuf. **7**, 20 (2015)
15. J.P. Oliveira, T.G. Santos, R.M. Miranda, Prog. Mater. Sci. **107**, 100590 (2020)
16. F. Wang, S. Williams, M. Rush, Int. J. Adv. Manuf. Tech. **57**, 597 (2011)
17. L. Ren, H. Gu, W. Wang, S. Wang, C. Li, Z. Wang, Y. Zhai, P. Ma, Met. Mater. Int. **27**, 68 (2021)
18. H.J. Yi, J.W. Kim, Y.L. Kim, S. Shin, Met. Mater. Int. **26**, 1235 (2020)
19. R.B. Song, J.Y. Xiang, D.P. Hou, J. Iron Steel Res. Int. **18**, 53 (2011)
20. B. Senior, Mater. Sci. Eng. **100**, 219 (1988)
21. S. Suryakumar, K.P. Karunakaran, U. Chandrasekhar, M.A. Somashekara, P. I. Mech. Eng. B J. Eng. **227**, 1138 (2013)
22. W. Jin, C. Zhang, S. Jin, Y. Tian, D. Wellmann, W. Liu, Appl. Sci. **10**, 1563 (2020)
23. A.R. Kannan, S.M. Kumar, R. Pramod, N.P. Kumar, N.S. Shanmugam, Y. Palguna, Sci. Technol. Weld. Joi. **26**, 47 (2020)
24. J. Ge, T. Ma, W. Han, T. Yuan, T. Jin, H. Fu, R. Xiao, Y. Lei, J. Lin, Appl. Therm. Eng. **163**, 114335 (2019)
25. H. Zhao, G. Zhang, Z. Yin, L. Wu, J. Mater. Process. Tech. **211**, 488 (2011)
26. M. Saadatmand, R. Talemi, Frat. ed Integrita Strutt. **14**, 98 (2020)
27. S.N. Ahmad, Y.HP. Manurung, M.F. Mat, Z. Minggu, A. Jaffar, S. Pruller, M. Leitner, IOP Conf. Ser. Mat. Sci. **834**, 012083 (2020)
28. M.A. Somashekara, M. Naveenkumar, A. Kumar, C. Viswanath, S. Simhambhatla, Int. J. Adv. Manuf. Tech. **90**, 2009 (2017)
29. R. Pramod, S.M. Kumar, B. Girinath, A.R. Kannan, N.P. Kumar, N.S. Shanmugam, Weld. World. **64**, 1905 (2020)
30. A.H. Nickel, D.M. Barnett, F.B. Prinz, Mater. Sci. Eng. A **317**, 59 (2001)
31. P. Michaleris, Finite Elem. Anal. Des. **86**, 51 (2014)
32. F. Montevecchi, G. Venturini, A. Scippa, G. Campatelli, Procedia CIRP **55**, 109 (2016)
33. J. Goldak, A. Chakravarti, M. Bibby, Metall. Trans. B **15**, 299 (1984)
34. R. Tangestani, G.H. Farrahi, M. Shishegar, B.P. Aghchehkandi, S. Ganguly, A. Mehmanparast, J. Mater. Eng. Perform. **29**, 2073 (2020)
35. J. Ding, P. Colegrove, J. Mehnen, S. Ganguly, P.M. Sequeira Almeida, F. Wang, S. Williams, Comp. Mater. Sci. **50**, 3315 (2011)
36. W. Kim, K.S. Kim, H. Lee, K. Yoo, J. Mech. Sci. Technol. **30**, 1773 (2016)
37. P. Kyvelou, H. Slack, D.D. Mountanou, M.A. Wadee, T.B. Britton, C. Buchanan, L. Gardner, Mater. Design **192**, 108675 (2020)
38. A.V. Jebaraj, L.A. Kumar, C.R. Deepak, Procedia Eng. **173**, 883 (2017)
39. S.M. Kumar, N.S. Shanmugam, Mater. Res. Express **5**, 106524 (2018)

40. ASTM A240 / A240M - 20a, Standard specification for Chromium and Chromium-Nickel stainless steel plate, sheet, and strip for pressure vessels and for general applications (ASTM International, West Conshohocken, 2020)
41. H.K.D.H. Bhadeshia, in *Mathematical Modelling of Weld Phenomena 2*, ed. by H. Cerjak, H. Bhadeshia. Possible effects of stress on steel weld microstructures (Institute of Materials, London, 1995), p. 71
42. Z. Wang, T.A. Palmer, A.M. Beese, Acta Mater. **110**, 226 (2016)
43. B.E. Carroll, T.A. Palmer, A.M. Beese, Acta Mater. **87**, 309 (2015)
44. S.M. Kumar, S. Sankarapandian, N.S. Shanmugam, J. Braz. Soc. Mech. Sci. **42**, 292 (2020)
45. V. Manvatkar, A. De, T. DebRoy, Mater. Sci. Technol. **31**, 924 (2015)
46. K. Zhang, S. Wang, W. Liu, X. Shang, Mater. Design **55**, 104 (2014)
47. X. Wu, Mater. Sci. Technol. **23**, 631 (2007)
48. Z. Sun, X. Tan, S.B. Tor, C.K. Chua, NPG Asia Mater. **10**, 127 (2018)
49. S. Kou, *Welding Metallurgy*, 3rd edn. (Wiley, Hoboken, 2020), pp. 172–177
50. J.P. Oliveira, T.M. Curado, Z. Zeng, J.G. Lopes, E. Rossinyol, J.M. Park, N. Schell, F.M. Braz Fernandes, H.S. Kim, Mater. Design **189**, 108505 (2020)
51. M. Gong, Y. Meng, S. Zhang, Y. Zhang, X. Zeng, M. Gao, Addit. Manuf. **33**, 101180 (2020)
52. B. Xie, J. Xue, X. Ren, Metals **10**, 1 (2020)
53. A. Bandyopadhyay, M. Upadhyayula, K.D. Traxel, B. Onuike, Mater. Lett. **255**, 126541 (2019)
54. A.R. Kannan, S.M. Kumar, N.P. Kumar, N.S. Shanmugam, A.S. Vishnu, Y. Palguna, Mater. Lett. **274**, 127968 (2020)
55. L. Carneiro, B. Jalalahmadi, A. Ashtekar, Y. Jiang, Int. J. Fatigue **123**, 22 (2019)
56. L.C. Shen, X.H. Yang, J.R. Ho, P.C. Tung, C.K. Lin, Materials **13**, 1 (2020)
57. A.R. Kannan, N.S. Shanmugam, V. Rajkumar, M. Vishnukumar, Mater. Lett. **270**, 127680 (2020)
58. D. Hull, D.J. Bacon, *Introduction to Dislocations*, 5th edn. (Butterworth-Heinemann, Oxford, 2011), pp. 85–107
59. E. Folkhard, *Welding Metallurgy of Stainless Steels*, 1st edn. (Springer, Wien, New York, 1988), pp. 112–114
60. A. Hussein, L. Hao, C. Yan, R. Everson, Mater. Design **52**, 638 (2013)
61. H. Zhao, G. Zhang, Z. Yin, L. Wu, J. Mater. Process. Tech. **212**, 276 (2012)
62. J. Gu, J. Ding, S.W. Williams, H. Gu, P. Ma, Y. Zhai, J. Mater. Process. Tech. **230**, 26 (2016)
63. R. Xie, G. Chen, Y. Zhao, S. Zhang, W. Yan, X. Lin, Q. Shi, J. Manuf. Process. **38**, 494 (2019)
64. B. Zheng, Y. Zhou, J.E. Smugeresky, J.M. Schoenung, E.J. Lavernia, Metall. Mater. Trans. A **39**, 2228 (2008)

Publisher's Note Springer Nature remains neutral with regard to jurisdictional claims in published maps and institutional affiliations.